Three-body dynamics in a (1+1)-dimensional relativistic self-gravitating system

J. J. Malecki* and R. B. Mann[†]

Department of Physics, University of Waterloo, Waterloo, Ontario, Canada N2L 3G1
(Received 19 June 2003; published 10 June 2004)

The results of our study of the motion of a three particle, self-gravitating system in general relativistic lineal gravity is presented for an arbitrary ratio of the particle masses. We derive a canonical expression for the Hamiltonian of the system and discuss the numerical solution of the resulting equations of motion. This solution is compared to the corresponding nonrelativistic and post-Newtonian approximation solutions so that the dynamics of the fully relativistic system can be interpreted as a correction to the one-dimensional Newtonian self-gravitating system. We find that the structure of the phase space of each of these systems yields a large variety of interesting dynamics that can be divided into three distinct regions: annulus, pretzel, and chaotic; the first two being regions of quasiperiodicity while the latter is a region of chaos. By changing the relative masses of the three particles we find that the relative sizes of these three phase space regions changes, and that this deformation can be interpreted physically in terms of the gravitational interactions of the particles. Furthermore, we find that many of the interesting characteristics found in the case where all of the particles share the same mass also appear in our more general study. We find that there are additional regions of chaos in the unequal mass system which are not present in the equal mass case. We compare these results to those found in similar systems.

I. INTRODUCTION

The calculation of the motion of N particles under a specified, mutual force is one of the oldest problems in physics, commonly referred to as the N-body problem. This problem occurs frequently in many distinct subfields and remains an active area of research. When the specified force is that of Newtonian gravity in three spatial dimensions, a closed form solution of the motion can be obtained for $N=2$. This is not true for $(3+1)$-dimensional general relativistic gravity, however, due to the existence of energy dissipation in the form of gravitational radiation. All attempts to calculate the motion of more than one particle in $(3+1)$ general relativity have required some form of approximation.

Considerable progress in this area of research has been made recently by reducing the number of spatial dimensions from three to one. These lower-dimensional theories provide a simpler prototype for their higher-dimensional counterparts. Furthermore, for Newtonian gravity, one-dimensional self-gravitating systems (OGS's) have proven to be very useful in modeling many diverse physical systems. For example, it has been found that there exist stable core-halo structures in the OGS phase space that are reminiscent of those found in globular clusters [1]. These structures consist of a dense core of particles near equilibrium surrounded by a cloud of high kinetic energy particles that interact very weakly with the core. The OGS also models the dynamics of flat, parallel sheets colliding along a perpendicular axis [2] and the motion of stars interacting with a highly flattened galaxy [3]. More specifically, the three-particle OGS has been found to

model the motion of a billiard colliding with a wedge in a uniform gravitational field [2] two elastically colliding billiard balls in a uniform gravitational field [4], and a bound state of three quarks to form a "linear baryon" [5]. There are still many open questions about the OGS concerning its ergodic behavior, the conditions (if any) under which equipartition of energy is attained, whether or not it can reach a true equilibrium configuration from arbitrary initial conditions, and the appearance of fractal behavior [6].

In a relativistic context, reduction of the number of spatial dimensions results in an absence of gravitational radiation while retaining most (if not all) of the remaining conceptual features of relativistic gravity. Consequently, one might hope to obtain insight into the nature of relativistic dynamical gravitational systems at the classical (and perhaps even quantum) level in a wide variety of physical situations by studying the relativistic OGS, or ROGS.

Comparatively little has been known about the ROGS (even for $N=2$) until quite recently, when a prescription for obtaining its Hamiltonian from a generally covariant, minimally coupled action was obtained [7]. In the nonrelativistic limit $(c\rightarrow\infty)$, the Hamiltonian reduces to that of the OGS. This opened up the possibility of extending the insights of the OGS into the relativistic regime, and indeed, considerable progress has been made. Exact, closed-form solutions to the two-body problem have been obtained [8]. These have been extended to include both a cosmological constant [9,10] and electromagnetic interactions [11], and a new exact solution to the static-balance problem has been obtained [12]. In the N-body case, the Hamiltonian can be obtained as a series expansion in inverse powers of the speed of light c to arbitrary order and a complete derivation of the partition and single-particle distribution functions has been found in both the canonical and microcanonical ensembles [13] providing

*Email address: jjmaleck@uwaterloo.ca
[†]Email address: mann@avatar.uwaterloo.ca

interesting information concerning the influence of relativistic effects on self-gravitating systems. Very recently, formulation of the ROGS has been extended to circular topologies [14] (forbidden for the OGS), and a new N-body dynamical equilibrium solution has been found [15]. An exact expression for the relativistic, three-body Hamiltonian has been calculated and the motion of three equal-mass particles has been extensively studied [16,17]; these results are summarized in Sec. V A.

In this paper, we will generalize the study of the motion of three particles to include the unequal mass case. We work with a two-dimensional (2D) theory of gravity on a line (lineal gravity) that models 4D general relativity in that it sets the Ricci scalar R equal to the trace of the stress energy of prescribed matter fields and sources. Hence, as in $(3+1)$ dimensions, the evolution of space-time curvature is governed by the matter distribution, which in turn is governed by the dynamics of space-time [18]. Sometimes referred to as $R = T$ theory, it is a particular member of a broad class of dilaton gravity theories formulated on a line. What singles it out for consideration is its consistent nonrelativistic (i.e., $c \rightarrow \infty$) limit [18] which is, in general, a problematic limit for a generic $(1+1)$-dimensional theory of gravity [19]. Consequently it contains each of the aforementioned nonrelativistic self-gravitating systems as special cases. Furthermore, it reduces to Jackiw-Teitelboim (JT) theory [20] when the stress energy is that of a cosmological constant.

We have found that the best way to study the motion of three particles is to work in the canonical formalism. By expressing the action in canonical variables we are able to determine the Hamiltonian as a spatial integral of the second derivative of the dilaton field. This field is determined by the constraint equations derived from the action which can be solved by matching the solution of the field across each of the three particles. The result is a transcendental equation containing the Hamiltonian and expressed in terms of the remaining degrees of freedom, that is, the two mutual separations of the particles and their conjugate momenta. From this transcendental equation we obtain the canonical equations of motion, which are then solved numerically.

Through a change of coordinates, the Newtonian, three-particle OGS can be shown to be isomorphic to the motion of a single particle in a linear, hexagonal well potential. By applying this same change of variables to the three-particle ROGS we find an analogous hexagonal potential where the sides of the hexagonal cross section are curved outwards and the sides of the well no longer increase linearly with increasing particle separation. We find that, by changing the relative masses of the particles, the shape of the hexagonal cross section in both the Newtonian and relativistic systems is expanded or contracted perpendicular to one of the lines connecting opposite vertices. This change of variables simplifies the analysis of the motion significantly and is used throughout to extract useful information from both the three-particle OGS and ROGS.

As in Ref. [17] we consider three distinct three-body, self-gravitating systems: the nonrelativistic case (N) which has been extensively studied in many different contexts [2,4,5,21],[1] the fully relativistic case (R) described above, and a post-Newtonian expansion (pN) of the R system, truncated to leading order in c^{-2}. While exact relativistic solutions of the N-body problem have only been found for $N = 2,3$, the post-Newtonian expansion has been found for all finite values of N up to any order of accuracy [7]. Both the R and pN systems reduce to the N system in the limit $c \rightarrow \infty$.

In Sec. II we outline the canonical reduction procedure of Ref. [17] that leads to the relativistic Hamiltonian expression and the resulting canonical equations of motion. Some general properties of each of the systems are then discussed in Sec. III, focussing on the character of the associated potential energy functions of each. The method for numerically solving the equations of motion is described in section IV and the results of this numerical solution presented in Sec. V. These results are then summarized and discussed in Sec. VI, which concludes with a comment on areas of further research interest.

II. HAMILTONIAN FORMULATION OF THE RELATIVISTIC EQUATIONS OF MOTION

The general procedure for deriving the N-body Hamiltonian via canonical reduction is given in Refs. [8,10,17] and only a brief description will be given here.

The action for the gravitational field minimally coupled to N point particles in $(1+1)$ dimensions is given by

$$
I = \int d^2x \left[\frac{1}{2\kappa} \sqrt{-g} g^{\mu\nu} \left\{ \Psi R_{\mu\nu} + \frac{1}{2} \nabla_\mu \Psi \nabla_\nu \Psi \right\} \right.
$$
$$
\left. + \sum_{a=1}^{N} \int d\tau_a \left\{ -m_a \left(-g_{\mu\nu}(x) \frac{dz_a^\mu}{d\tau_a} \frac{dz_a^\nu}{d\tau_a} \right)^2 \right\} \delta^{(2)}[x - z_a(\tau_a)] \right],
$$
(1)

where $g_{\mu\nu}$ is the metric tensor with determinant g, $R_{\mu\nu}$ is the Ricci tensor, τ_a the proper time for the ath particle with mass m_a and position z_a, and $\kappa = 8\pi G/c^4$. We use ∇_μ to denote the covariant derivative associated with $g_{\mu\nu}$. The scalar (dilaton) field Ψ has been incorporated because the classical Einstein-Hilbert action in $(1+1)$ dimensions is trivial due to the vanishing of the Einstein tensor. This action describes a self-gravitating system of N particles without collisional terms (i.e., the particles pass through each other).

From Eq. (1) one can derive the following field equations:

$$
R - g^{\mu\nu} \nabla_\mu \nabla_\nu \Psi = 0,
$$
(2)

---

[1]These studies examine the three-body problem in a classical potential obtained by solving Poisson's equation in one spatial dimension. The potential linearly depends on the separation of the particles as seen in Eq. (20). The chaotic properties of the one-dimensional three-body problem with a potential that depends inversely on the separation (as in three dimensions) have been studied in Ref. [22].

$$\frac{1}{2}\nabla_\mu\Psi\nabla_\nu\Psi - \frac{1}{4}g_{\mu\nu}\nabla^\lambda\Psi\nabla_\lambda\Psi + g_{\mu\nu}\nabla^\lambda\nabla_\lambda\Psi - \nabla_\mu\nabla_\nu\Psi = \kappa T_{\mu\nu},$$

$$(3)$$

$$m_a\left[\frac{d}{d\tau_a}\left\{g_{\mu\nu}(z_a)\frac{dz_a^\nu}{d\tau_a}\right\} - \frac{1}{2}g_{\nu\lambda,\mu}(z_a)\frac{dz_a^\nu}{d\tau_a}\frac{dz_a^\lambda}{d\tau_a}\right] = 0, \quad (4)$$

where

$$T_{\mu\nu} = \sum_a m_a\int d\tau_a\frac{1}{\sqrt{-g}}g_{\mu\sigma}g_{\nu\rho}\frac{dz_a^\sigma}{d\tau_a}\frac{dz_a^\rho}{d\tau_a}\delta^{(2)}[x - z_a(\tau_a)]$$

$$(5)$$

is the stress-energy tensor for the N particles and is conserved via Eq. (3). Inserting the trace of Eq. (3) into Eq. (2) we obtain

$$R = \kappa T^\mu_\mu. \quad (6)$$

The fact that we retain this simple relation between the geometry of space-time and the matter, analogous to the Einstein field equations, is the motivation for choosing the dilaton coupling in Eq. (1).

Equations (4) and (6) form an $(N+1)$-dimensional system that can be solved for the single metric degree of freedom and the N particle degrees of freedom. Equation (3) relates the evolution of the dilaton field to the evolution of the point masses.

To arrive at a Hamiltonian theory we begin by writing the metric as

$$ds^2 = -N_0^2(x,t)dt^2 + \gamma\left(dx + \frac{N_1(x,t)}{\gamma}dt\right)^2, \quad (7)$$

where N_0 and N_1 are the lapse and shift functions which act as Lagrange multipliers for the resulting constraints of the Hamiltonian system and γ is the single metric degree of freedom.

By also defining p_a, π, and Π to be the conjugate momentum of z_a, γ, and Ψ, respectively, one can canonically reduce the action to the form [7]

$$I = \int d^2x\left\{\sum_a p_a\dot{z}_a\delta(x - z_a) + \frac{1}{\kappa}\Delta\Psi\right\}, \quad (8)$$

upon eliminating the constraints and choosing the coordinate conditions $\gamma=1$ and $\Pi=0$. Here we use Δ to denote $\partial^2/\partial x^2$ and a dot to denote $\partial/\partial t$. With the action in this form, we recognize the second term $\mathcal{H}=-1/\kappa\Delta\Psi$ as the Hamiltonian density and can immediately write down the Hamiltonian for N particles as

$$H = \int dx\mathcal{H} = -\frac{1}{\kappa}\int dx\Delta\Psi, \quad (9)$$

where Ψ is a function of z_a and p_a and can be determined from the solution to the constraint equations which now take the form

$$\Delta\Psi - \frac{1}{4}(\Psi')^2 + \kappa^2\pi^2 + \kappa\sum_a\sqrt{p_a^2 + m_a^2}\delta(x - z_a) = 0,$$

$$(10)$$

$$2\pi' + \sum_a p_a\delta(x - z_a) = 0, \quad (11)$$

where a prime denotes $\partial/\partial x$.

The solution of Eqs. (9)–(11) for the three-particle case is given in Ref. [17] and will not be reproduced here in detail. The basic procedure involves choosing a specific configuration of the three particles and solving Eqs. (10) and (11) in the region between each particle. The constants of integration are then determined by demanding that Ψ and Ψ' remain finite and coincide at the position of the particles. This gives an implicit equation for the Hamiltonian H for the specified particle configuration and the Hamiltonian for a general configuration is obtained by permutation of the particle indices (1, 2, and 3).

This implicit equation for the Hamiltonian can be expressed as

$$L_1L_2L_3 = \mathcal{M}_{12}\mathcal{M}_{21}L_3^*e^{(\kappa/4)s_{12}[(L_1+\mathcal{M}_{12})z_{13}-(L_2+\mathcal{M}_{21})z_{23}]}$$
$$+ \mathcal{M}_{23}\mathcal{M}_{32}L_1^*e^{(\kappa/4)s_{23}[(L_2+\mathcal{M}_{23})z_{21}-(L_3+\mathcal{M}_{32})z_{31}]}$$
$$+ \mathcal{M}_{31}\mathcal{M}_{13}L_2^*e^{(\kappa/4)s_{31}[(L_3+\mathcal{M}_{31})z_{32}-(L_1+\mathcal{M}_{13})z_{12}]},$$

$$(12)$$

or more compactly

$$L_1L_2L_3 = \frac{1}{2}\sum_{ijk}|\epsilon^{ijk}|\mathcal{M}_{ij}\mathcal{M}_{ji}L_k^*e^{(\kappa/4)s_{ij}[(L_i+\mathcal{M}_{ij})z_{ik}-(L_j+\mathcal{M}_{ji})z_{jk}]},$$

$$(13)$$

where

$$\mathcal{M}_{ij} = M_i - \epsilon p_i s_{ij}, \quad M_i = \sqrt{p_i^2 + m_i^2}, \quad (14)$$

$$L_i = H - M_i - \epsilon\left(\sum_j p_j s_{ji}\right), \quad L_i^* = \left(1 - \prod_{j<k\neq i}s_{ij}s_{ik}\right)M_i + L_i,$$

$$(15)$$

with $z_{ij}=(z_i-z_j)$, $s_{ij}=\text{sgn}(z_{ij})$, and ϵ^{ijk} is the three-dimensional Levi-Civita tensor. The discrete parameter $\epsilon = \pm 1$ is a constant of integration that flips sign under time reversal. This provides a measure of the flow of time of the gravitational field relative to the particle momenta.

Although we cannot obtain an explicit expression for the Hamiltonian, we are able to derive the equations of motion explicitly by partially differentiating Eq. (13) implicitly with

respect to z_a and p_a and solving for $\partial H/\partial z_a$ and $\partial H/\partial p_a$, respectively. From Hamilton's equations

$$\dot{z}_a = \frac{\partial H}{\partial p_a}, \qquad (16)$$

$$\dot{p}_a = -\frac{\partial H}{\partial z_a}, \qquad (17)$$

we can obtain the equations of motion.

For example, for $a=1$, Eqs. (16) and (17) become

$$
\begin{aligned}
&\dot{z}_1\Bigg\{L_2L_3 + L_1L_3 + L_1L_2 - [M_2 - \epsilon p_2 s_{21}][M_1 - \epsilon p_1 s_{12}]\left[1 + \frac{\kappa}{4}L_3^*|z_{12}|\right]e^{(\kappa/4)s_{12}[(L_1+\mathcal{M}_{12})z_{13}-(L_2+\mathcal{M}_{21})z_{23}]} - [M_3 - \epsilon p_3 s_{31}][M_1 - \epsilon p_1 s_{13}]\\
&\times\left[1 + \frac{\kappa}{4}L_2^*|z_{13}|\right]e^{(\kappa/4)s_{31}[(L_3+\mathcal{M}_{31})z_{32}+(L_1+\mathcal{M}_{13})z_{12}]} - [M_2 - \epsilon p_2 s_{23}][M_3 - \epsilon p_3 s_{32}]\left[1 + \frac{\kappa}{4}L_1^*|z_{23}|\right]e^{(\kappa/4)s_{23}[(L_3+\mathcal{M}_{32})z_{13}-(L_2+\mathcal{M}_{23})z_{12}]}\Bigg\}\\
&=[M_2 - \epsilon p_2 s_{21}]\left[\left(\frac{\partial M_1}{\partial p_1} - \epsilon s_{12}\right)L_3^* - (M_1 - \epsilon p_1 s_{12})\left\{\epsilon s_{13} + \frac{\kappa}{4}L_3^*(\epsilon z_{12})\right\}\right]e^{(\kappa/4)s_{12}[(L_1+\mathcal{M}_{12})z_{13}-(L_2+\mathcal{M}_{21})z_{23}]} + [M_3 - \epsilon p_3 s_{31}]\left[\left(\frac{\partial M_1}{\partial p_1}\right.\right.\\
&\left.\left.- \epsilon s_{13}\right)L_2^* - (M_1 - \epsilon p_1 s_{13})\left\{\epsilon s_{12} + \frac{\kappa}{4}L_2^*(\epsilon z_{13})\right\}\right]e^{(\kappa/4)s_{13}[(L_1+\mathcal{M}_{13})z_{12}+(L_3+\mathcal{M}_{31})z_{23}]} + [M_2 - \epsilon p_2 s_{23}][M_3 - \epsilon p_3 s_{32}]\left[-s_{12}s_{13}\frac{\partial M_1}{\partial p_1}\right.\\
&\left.+ \frac{\kappa}{4}s_{23}L_1^*[\epsilon|z_{12}| - \epsilon|z_{13}|]\right]e^{(\kappa/4)s_{23}[(L_3+\mathcal{M}_{32})z_{13}-(L_2+\mathcal{M}_{23})z_{12}]} + \frac{\partial M_1}{\partial p_1}L_2L_3 + \epsilon(s_{12}L_1L_3 + s_{13}L_2L_1),
\end{aligned}
\tag{18}
$$

and

$$
\begin{aligned}
&\dot{p}_1\Bigg\{L_2L_3 + L_1L_3 + L_1L_2 - [M_2 - \epsilon p_2 s_{21}][M_1 - \epsilon p_1 s_{12}]\left[1 + \frac{\kappa}{4}L_3^*|z_{12}|\right]e^{(\kappa/4)s_{12}[(L_1+\mathcal{M}_{12})z_{13}-(L_2+\mathcal{M}_{21})z_{23}]} - [M_3 - \epsilon p_3 s_{31}][M_1 - \epsilon p_1 s_{13}]\\
&\times\left[1 + \frac{\kappa}{4}L_2^*|z_{13}|\right]e^{(\kappa/4)s_{13}[(L_1+\mathcal{M}_{13})z_{12}+(L_3+\mathcal{M}_{31})z_{23}]} - [M_2 - \epsilon p_2 s_{23}][M_3 - \epsilon p_3 s_{32}]\left[1 + \frac{\kappa}{4}L_1^*|z_{23}|\right]\\
&\times e^{(\kappa/4)s_{23}[(L_2+\mathcal{M}_{23})z_{21}-(L_3+\mathcal{M}_{32})z_{31}]}\Bigg\}\\
&=[M_2 - \epsilon p_2 s_{21}][M_1 - \epsilon p_1 s_{12}]\left[\frac{\kappa}{4}s_{12}L_3^*[H + \epsilon(p_2 - p_1)s_{12} + \epsilon p_3 s_{13}]\right]e^{(\kappa/4)s_{12}[(L_1+\mathcal{M}_{12})z_{13}-(L_2+\mathcal{M}_{21})z_{23}]}\\
&+ [M_3 - \epsilon p_3 s_{31}][M_1 - \epsilon p_1 s_{13}]\left[\frac{\kappa}{4}s_{13}L_2^*[H + \epsilon p_2 s_{12} + \epsilon(p_3 - p_1)s_{13}]\right]e^{(\kappa/4)s_{13}[(L_1+\mathcal{M}_{13})z_{12}+(L_3+\mathcal{M}_{31})z_{23}]}\\
&+ [M_2 - \epsilon p_2 s_{23}][M_3 - \epsilon p_3 s_{32}]\left[\frac{\kappa}{4}s_{23}L_1^*p_1(s_{12} - s_{13})\right]e^{(\kappa/4)s_{23}[(L_3+\mathcal{M}_{32})z_{13}-(L_2+\mathcal{M}_{23})z_{12}]}.
\end{aligned}
\tag{19}
$$

The equations for $a=2,3$ are similar and will be omitted here.

III. GENERAL PROPERTIES OF THE THREE-BODY SYSTEM

Before we go on to solve the equations of motion, it is instructive to consider some general characteristics of the three-body system described by the determining Eq. (12) and its associated nonrelativistic and post-Newtonian counterparts.

To compare the relativistic motion to that predicted classically, we introduce the Newtonian N particle Hamiltonian in $(1+1)$ dimensions

$$H_N = \sum_a \frac{p_a^2}{2m_a} + \pi G\sum_a\sum_b m_a m_b|z_{ab}|, \qquad (20)$$

where $z_{ab} = z_a - z_b$ as before. We shall refer to this as the Newtonian or N system.

A post-Newtonian approximation of the general N-body Hamiltonian has been found [7] and is given here up to order c^{-2}:

$$H_{pN} = c^2 \sum_a m_a + \sum_a \frac{p_a^2}{2m_a} + \frac{\kappa c^4}{8} \sum_a \sum_b m_a m_b |z_{ab}|$$
$$+ \frac{\epsilon \kappa c^3}{8} \sum_a \sum_b (m_a p_b - m_b p_a)(z_{ab}) - c \sum_a \frac{p_a^4}{8m_a^3}$$
$$+ \frac{\kappa c^2}{8} \sum_a \sum_b \left(m_a \frac{p_a^2}{m_b} |z_{ab}| - p_a p_b |z_{ab}| \right)$$
$$+ \frac{1}{4} \left(\frac{\kappa}{4} \right)^2 c^6 \sum_a \sum_b \sum_c m_a m_b m_c (|z_{ab}||z_{ac}| + z_{ab} z_{ac}).$$

$$(21)$$

If we rescale (21) to remove the constant $\sum_a m_a c^2$ term and take the limit $c \to \infty$ then it is clear that we retrieve the Newtonian result (20).

However, the coordinates z_a and p_a are not necessarily the most natural coordinates to use to describe the post-Newtonian system. The reason is that the fourth term on the right hand side of Eq. (21) is proportional to c^{-1}. In $(3+1)$ dimensions, terms in odd powers of c^{-1} are associated with gravitational radiation, but, in $(1+1)$ dimensions, there are not enough degrees of freedom to allow for the existence of gravitational radiation, and such terms are artifacts of the choice of canonical variables.

Indeed, as in Ref. [7], we can remove the c^{-1} term by performing the canonical transformation

$$z_a \to \tilde{z}_a = z_a, \qquad (22)$$

$$p_a \to \tilde{p}_a = p_a - \frac{\epsilon \kappa}{4} \sum_b m_a m_b z_{ab}, \qquad (23)$$

after which, Eq. (21) becomes

$$\tilde{H}_{pN} = c^2 \sum_a m_a + \sum_a \frac{\tilde{p}_2^a}{2m_a} + \frac{\kappa c^4}{8} \sum_a \sum_b m_a m_b |\tilde{z}_{ab}| - c \sum_a \frac{\tilde{p}_4^a}{8m_a^3}$$
$$+ \frac{\kappa c^2}{8} \sum_a \sum_b \left(m_a \frac{\tilde{p}_2^a}{m_b} |\tilde{z}_{ab}| - \tilde{p}_a \tilde{p}_b |\tilde{z}_{ab}| \right)$$
$$+ \frac{1}{4} \left(\frac{\kappa}{4} \right)^2 c^6 \sum_a \sum_b \sum_c m_a m_b m_c (|\tilde{z}_{ab}||\tilde{z}_{ac}| - \tilde{z}_{ab} \tilde{z}_{ac}), \quad (24)$$

where $\tilde{z}_{ab} = \tilde{z}_a - \tilde{z}_b$. Since Eq. (24) uses different coordinates than Eqs. (20) and (12) it is important to distinguish between the two expressions for the post-Newtonian Hamiltonian. We will refer to the system described by Eq. (21) as the untransformed post-Newtonian system, or UpN system, and the system described by Eq. (24) simply as the post-Newtonian or pN system. Note that only the pN system was studied in Ref. [17]. To complete our nomenclature, the fully relativistic system will be denoted as the R system. Unless otherwise stated, the Newtonian system will be assumed to have been

rescaled so that $H(z_{ab}=0, p_a=0) = (m_1 + m_2 + m_3)c^2$ in order to properly compare it to the pN and R cases.

In order to simplify our analysis we will adopt the convention of Refs. [5,17] and define the following canonical coordinates:

$$\rho = \frac{1}{\sqrt{2}}(z_1 - z_2), \quad \lambda = \frac{1}{\sqrt{6}}(z_1 + z_2 - 2z_3), \quad Z = z_1 + z_2 + z_3,$$

$$(25)$$

with conjugate momenta

$$p_\rho = \frac{1}{\sqrt{2}}(p_1 - p_2), \quad p_\lambda = \frac{1}{\sqrt{6}}(p_1 + p_2 - 2p_3),$$

$$p_Z = \tfrac{1}{3}(p_1 + p_2 + p_3). \qquad (26)$$

In the nonrelativistic limit, Z and p_Z are related to the center of mass and its conjugate momentum. While the equivalence principle does not allow us to arbitrarily set Z in the relativistic case, we can, without loss of generality, choose p_Z to vanish. The consequence of this is that we can explicitly express p_1, p_2, and p_3 in terms of the newly defined momenta (26) but can only express the *separations* of the particles z_{ab} explicitly in terms of the new coordinates (25). This gives us the following relations:

$$z_{12} = \sqrt{2}\rho, \quad z_{13} = \frac{1}{\sqrt{2}}(\sqrt{3}\lambda + \rho), \quad z_{23} = \frac{1}{\sqrt{2}}(\sqrt{3}\lambda - \rho),$$

$$(27)$$

$$p_1 = \frac{1}{\sqrt{6}}p_\lambda + \frac{1}{\sqrt{2}}p_\rho, \quad p_2 = \frac{1}{\sqrt{6}}p_\lambda - \frac{1}{\sqrt{2}}p_\rho, \quad p_3 = -\sqrt{\frac{2}{3}}p_\lambda.$$

$$(28)$$

All of the Hamiltonian expressions (12), (20), (21), and (24) do not depend on Z or p_Z and so these variables are irrelevant. Expressions for Eqs. (12), (20), and (24) in terms of the new coordinates are given in Ref. [17] for the case when $m_1 = m_2 = m_3$. The corresponding expressions for unequal masses are very cumbersome and will not be reproduced here.

By defining the potential of each system as $V(\rho, \lambda) = H(p_\rho = 0, p_\lambda = 0)$ we can compare some of the different characteristics of the three systems. In ρ-λ coordinates the N potential becomes

$$V_N = m_1 + m_2 + m_3 + \frac{\kappa}{4\sqrt{2}}(2m_1 m_2 |\rho| + m_1 m_3 |\sqrt{3}\lambda + \rho|$$
$$+ m_2 m_3 |\sqrt{3}\lambda - \rho|), \qquad (29)$$

where we have rescaled the Hamiltonian as described above (with c henceforth set to unity unless explicitly stated otherwise). The UpN potential is given as

$$V_{pN} = m_1 + m_2 + m_3 + \frac{\kappa}{4\sqrt{2}}(2m_1 m_2|\rho| + m_1 m_3|\sqrt{3}\lambda + \rho|$$
$$+ m_2 m_3|\sqrt{3}\lambda - \rho|) + \frac{1}{2}\left(\frac{\kappa}{4}\right)^2 m_1 m_2 m_3[4\rho^2 + (\sqrt{3}\lambda + \rho)^2$$
$$+ (\sqrt{3}\lambda - \rho)^2 + (1 + s_\rho s_1)|\rho||\sqrt{3}\lambda + \rho|]$$
$$+ \frac{1}{2}\left(\frac{\kappa}{4}\right)^2 m_1 m_2 m_3\Big[(1 - s_\rho s_2)|\rho||\sqrt{3}\lambda - \rho| + \frac{1}{2}(1 + s_1 s_2)$$
$$\times |\sqrt{3}\lambda + \rho||\sqrt{3}\lambda - \rho|\Big] \tag{30}$$

and the pN potential is

$$\widetilde{V}_{pN} = m_1 + m_2 + m_3 + \frac{\kappa}{4\sqrt{2}}(2m_1 m_2|\widetilde{\rho}| + m_1 m_3|\sqrt{3}\widetilde{\lambda} + \widetilde{\rho}|$$
$$+ m_2 m_3|\sqrt{3}\widetilde{\lambda} - \widetilde{\rho}|) + \frac{1}{2}\left(\frac{\kappa}{4}\right)^2 m_1 m_2 m_3\Bigg[(1 - \widetilde{s}_\rho \widetilde{s}_1)$$
$$\times |\widetilde{\rho}||\sqrt{3}\widetilde{\lambda} + \widetilde{\rho}| + (1 + \widetilde{s}_\rho \widetilde{s}_2)|\widetilde{\rho}||\sqrt{3}\widetilde{\lambda} - \widetilde{\rho}| + \frac{1}{2}(1 - \widetilde{s}_1 \widetilde{s}_2)$$
$$\times |\sqrt{3}\widetilde{\lambda} + \widetilde{\rho}||\sqrt{3}\widetilde{\lambda} - \widetilde{\rho}|\Bigg], \tag{31}$$

where $\widetilde{\rho}$ and $\widetilde{\lambda}$ are defined as in Eq. (25) using the $\widetilde{z}_a$ coordinates of Eq. (22). Here we have defined $s_\rho = \text{sgn}(\rho)$, $s_1 = \text{sgn}(\sqrt{3}\lambda + \rho)$, and $s_2 = \text{sgn}(\sqrt{3}\lambda - \rho)$ and the $\widetilde{s}$ terms are defined similarly in terms of $\widetilde{\rho}$ and $\widetilde{\lambda}$. The exact relativistic potential can be calculated from Eq. (12) to be

$$(V_R - m_1)(V_R - m_2)(V_R - m_3)$$
$$= m_1 m_2(V_R - s_1 s_2 m_3)$$
$$\times \exp\left[\frac{\kappa}{2\sqrt{2}}V_R|\rho|\right] + m_1 m_3(V_R + s_\rho s_2 m_2)$$
$$\times \exp\left[\frac{\kappa}{4\sqrt{2}}V_R|\sqrt{3}\lambda + \rho|\right] + m_2 m_3(V_R - s_\rho s_1 m_1)$$
$$\times \exp\left[\frac{\kappa}{4\sqrt{2}}V_R|\sqrt{3}\lambda - \rho|\right]. \tag{32}$$

An extensive comparison between the different potentials has been given in Ref. [17] for the case where the particle masses are equal and so here we wish to focus on the changes to the potential due to changes in the relative masses of the three particles.

A cross section of each of the potentials at a fixed value of V is shown in Fig. 1 for the case where all particles have the same mass. All of the potentials share a certain hexagonal symmetry in that they are all smooth except along the lines

$$\rho = 0, \tag{33}$$

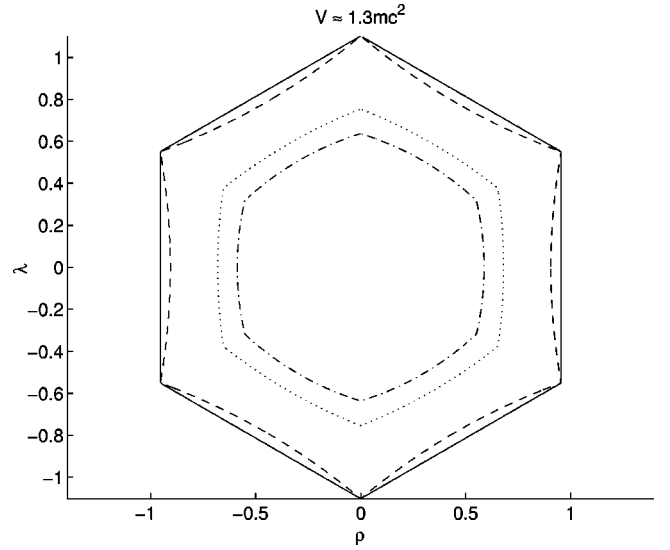$$\rho + \sqrt{3}\lambda = 0, \tag{34}$$

FIG. 1. A cross section of the four potentials at $V \approx 1.3 M_{tot}c^2$ in the case that all three particles have the same mass. N—solid, pN—dashed, UpN—dotted, R—dash dotted. ρ and λ are dimensionless variables defined using the dimensionless positions $\hat{z}_i$ of Eq. (38).

$$\rho - \sqrt{3}\lambda = 0, \tag{35}$$

which correspond to $z_1 = z_2$, $z_1 = z_3$, and $z_2 = z_3$, respectively (i.e., the potential is not differentiable when two particles are coincident). This is true for all ratios of the masses of the particles.

The Newtonian potential is a distorted hexagonal well with sides that increase linearly with V. The hexagonal cross section at any value of V_N only has equal length sides when $m_1 = m_2 = m_3$. Figure 2 shows various cross sections of the
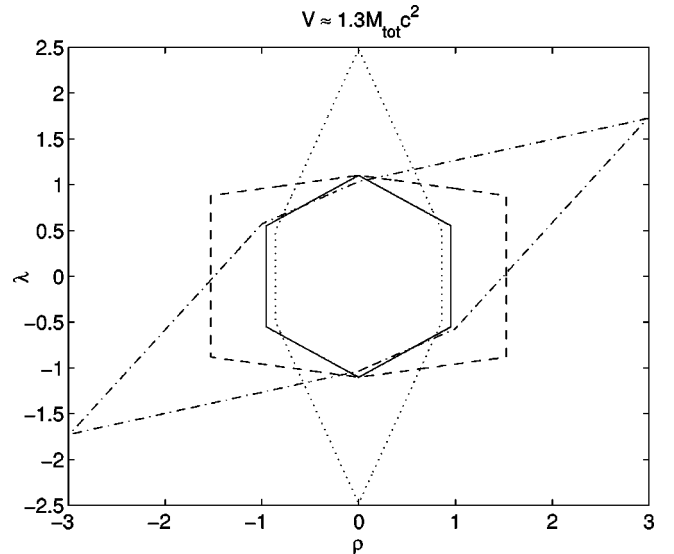

FIG. 2. Cross sections of the Newtonian potential at $V \approx 1.3 M_{tot}c^2$ for various mass ratios $m_1 : m_2 : m_3$. Solid—1:1:1; dashed—1:1:4; dotted—4:4:1; dash dotted—1:4:8. Note that all discontinuities lie on one of the three bisectors (33)–(35) regardless of the mass ratio. ρ and λ are dimensionless variables as in Fig. 1.
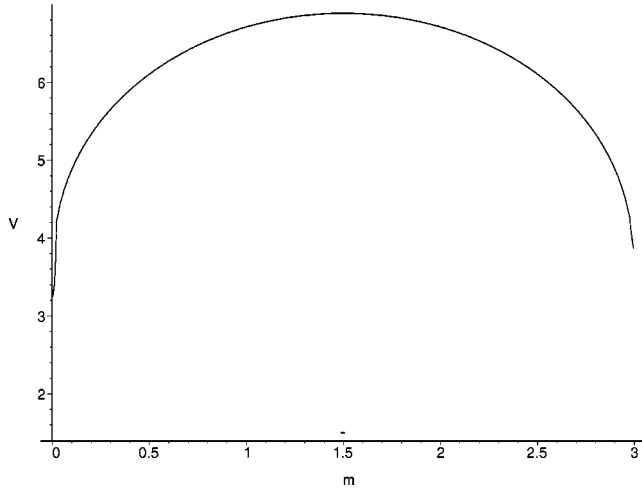
FIG. 3. Critical values of the relativistic potential V_R as a function of a given particle mass in units of M_{tot} (here set equal to 3). The maximum critical value occurs in the case when $m_j = M_{tot}/2$. The minimal value approaches the limit $V_R \simeq M_{\text{tot}}$ as $m_j \to 0$ or M_{tot}.

Newtonian potential at a fixed value of V for different mass ratios. We see that increasing the mass of particle 3 has the effect of expanding the hexagon away from the $\rho = 0$ bisector while decreasing the mass contracts the hexagonal cross section towards $\rho = 0$. Increasing and decreasing the mass of particles 1 or 2 has the same effect but the deformation is perpendicular to the $\rho - \sqrt{3}\lambda = 0$ or $\rho + \sqrt{3}\lambda = 0$, respectively. When all three particles have unequal mass, the hexagon is deformed as above with the magnitude of the deformation in each direction given by the relative values of the mass.

The relativistic potential is similar to the Newtonian potential except that the sides of the hexagon become concave. Furthermore, for small values of (ρ, λ), the relativistic potential increases much more rapidly than the Newtonian potential. However, at a value $\hat{V}_R$ such that

$$\ln\left(\frac{(\hat{V}_R - m_j)[\hat{V}_R - (M_{\text{tot}} - m_j)]}{(M_{\text{tot}} - m_j)m_j}\right)$$
$$= \hat{V}_R\left[\frac{1}{(\hat{V}_R - m_j)} + \frac{1}{[\hat{V}_R - (M_{\text{tot}} - m_j)]}\right] \quad (36)$$

(for $j = 1, 2$, or 3), the slope of the relativistic potential becomes infinite, after which the size of the distorted hexagon decreases like $(\ln V_R)/V_R$ with increasing V_R. In the equal mass case this yields a value $\hat{V}_R \approx 6.71197 mc^2$, where $m = M_{\text{tot}}/3$. For $m = M_{\text{tot}}/2$ we obtain $\hat{V}_R \approx 6.886\,682 mc^2$ which is the maximal possible critical value of the potential, and in the limits $m \to 0, M_{\text{tot}}$ we find $\hat{V}_R \to M_{\text{tot}}$. A plot of the critical values of the potential as a function of m_j is given in Fig. 3.

The overall shape of the relativistic potential is that of a distorted, hexagonal carafe. The distortion of the relativistic potential for different ratios of the particle masses is analogous to the Newtonian potential and can be seen in Fig. 4.

The untransformed post-Newtonian potential shares similar features with the relativistic potential in that the sides of
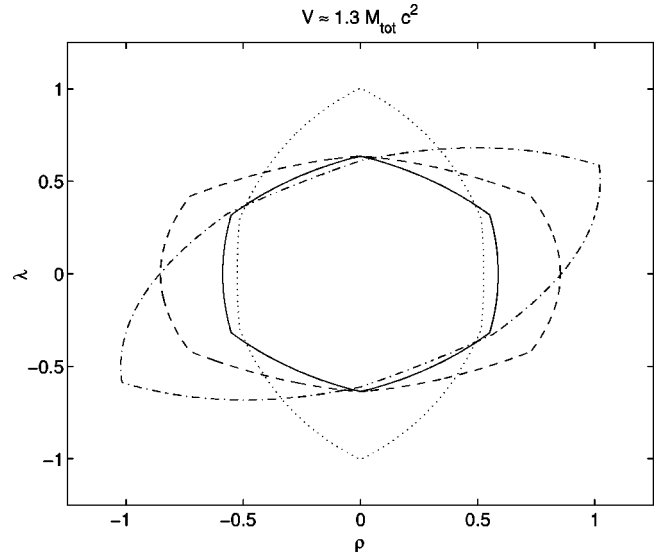

FIG. 4. Cross sections of the relativistic potential at $V \approx 1.3 M_{tot}c^2$ for different ratios of the particle masses. The correspondence between line style and ratio is the same as in Fig. 2. The deformation of the potential due to changing the mass ratio is the same as in the Newtonian case. The ρ and λ are dimensionless variables as in Fig. 1.

the distorted hexagonal cross section are concave outward. However, as one might expect, the potential increases less rapidly than the relativistic potential but still more rapidly than the Newtonian potential at small values of (ρ, λ). Furthermore, the sides of the well continue to increase quadratically with increasing (ρ, λ) without the slope ever going to infinity as in the relativistic case. Figure 5 shows a cross section of the untransformed post-Newtonian potential at a fixed value of V for different mass ratios.

The transformed post-Newtonian potential has a much different character than all of the potential energy functions discussed so far. The sides of the distorted hexagon become convex and the vertices are always coincident with the Newtonian potential at a fixed value of V. As V increases, the sides become more convex with respect to the Newtonian potential. Cross sections of this potential for different ratios of the particle masses at a fixed value of V can be seen in Fig. 5.

Finally, we note that the potential energy does not completely govern the motion in the R and pN cases as it does in the N case due to the momentum dependence of V in the former cases. Consequently, such comparison of the potentials is limited in the insight it can provide.

IV. METHODS FOR SOLVING THE EQUATIONS OF MOTION

The motion of the three particles under study is quite complex so we have adopted several methods to study the equations of motion. The most straight forward approach is to look at the position of each particle with respect to the center of mass $\sum m_a z_a$ as a function of time (where time will be explicitly defined shortly). Recall, however, that the
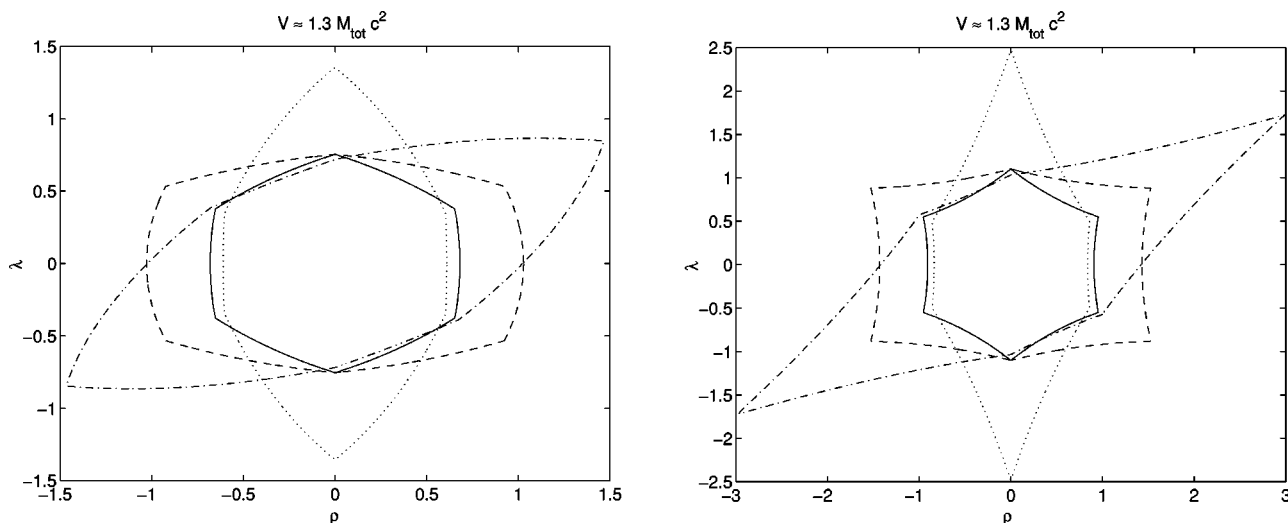
FIG. 5. Cross sections of both the untransformed (left) and transformed post-Newtonian potentials at $V \approx 1.3 M_{tot}c^2$ for various mass ratios. The correspondence between ratio and line is the same as in Fig. 2. The ρ and λ are dimensionless variables as in Fig. 1.

choice of the center of mass reference frame is arbitrary and is not necessarily stationary to an observer as it is in the Newtonian case.

Under the change of coordinates (25) and (26), the motion of the three particles is isomorphic to the motion of a single particle moving in the hexagonal well potential (29) in the Newtonian case. The situation is analogous in the fully relativistic and post-Newtonian cases except that the potentials become momentum dependent. So, as in Refs. [17,5], we focus on the trajectory of this particle, which we call the "hex particle," in the ρ-λ plane as an alternate way to analyze the motion.

As mentioned before, the bisectors (33)–(36) correspond to points where two of the particles are coincident. These bisectors divide the ρ-λ plane into six sextants corresponding to the six different configurations the three particles can assume. So, when the hex particle moves from one sextant to the next, this corresponds to two particles passing through each other. In the equal mass case, all six sextants are equivalent, and in the unequal mass case, opposite sextants correspond to the opposite configuration of particles [i.e. $(1,2,3) \rightarrow (3,2,1)$]. Further symmetries exist when two particles have the same mass.

An analogous system was studied by Lehtihet and Miller [2,21] who demonstrated that a self-gravitating Newtonian system of three particles in $(1+1)$ dimensions *with collisions* is equivalent to the motion of a particle in a uniform gravitational field colliding elastically with a wedge. The existence of particle collisions in our study of the N system would correspond to the hex particle being confined to a single sextant where it would reduce to the particle-wedge system. In this particle-wedge system, the equations of motion can be integrated between collisions of the particle with the wedge and a discrete mapping describing the radial and angular velocity of the particle at each collision can be used to describe the motion. The simplification to a discrete mapping allows one to calculate fixed points in phase space and evaluate their stability much more easily. Unfortunately, the equations of motion for the pN and R systems are much

more complex than in the Newtonian case and it is not clear how to create a discrete mapping between particle collisions.

Following Refs. [2,17] we define two types of motion: *A* motion, where two particles cross twice in succession; and *B* motion, where a single particle crosses each of the other two in succession. In (ρ,λ) space, after the hex particle has just crossed one of the bisectors, *A* motion would correspond to a crossing of the same bisector while *B* motion would correspond to it crossing a different bisector. In this way, one can describe the trajectory of the hex particle as a succession of *A* and *B* motions and develop a "symbol sequence" for a given trajectory. To simplify the notation, we use exponents to denote a number of repeats of a given type of motion so that the symbol sequence takes the form $\Pi_{i,j,k} (A^{m_i}B^{n_j})^{l_k}$, where $l_k, m_i, n_j \in Z^+$ and l_k is possibly infinite, in which case we denote it by an overbar [i.e., $\lim_{c \to \infty} (A^a B^b)^c \equiv \overline{A^a B^b}$]. Since the type of hex-particle motion at a given bisector depends on the previous bisector, we avoid ambiguity by saying that the first bisector crossing of the hex particle is undefined, and the symbol sequence begins at the second crossing. To aid in understanding this nomenclature we have listed the symbol sequence in the captions of all configuration space trajectories where the trajectory is easy to follow.

The above methods allow us to study and classify individual trajectories of the hex particle in the four dimensional $(\rho,\lambda,p_\rho,p_\lambda)$ phase space. In order to study some of the global structure of this phase space, we construct Poincaré maps. Since all of the Hamiltonians under study are time independent, the total energy of the system is a constant of motion and so the motion at a given energy is confined to a three-dimensional hypersurface in phase space. We can further reduce this to two dimensions by plotting the radial momentum p_R and the square of the angular momentum p_θ^2 of the hex particle each time it crosses one of the bisectors, as in Refs. [2,17]. This is known as the surface of section or Poincaré map.

In the equal mass case, all bisectors are equivalent and so p_R and p_θ^2 at each bisector can be plotted on the same surface of section, as in Refs. [17]. When the masses are unequal,

this procedure is not possible and one must distinguish between the different bisectors and the directions in which they cross. We have chosen to plot points on the Poincaré map each time the hex particle crosses the $\rho=0$ boundary in the positive angular direction (i.e., when $p_\theta>0$). In the case when $m_1=m_2$, particles 1 and 2 are indistinguishable and we may also plot (p_R,p_θ^2) each time the hex particle crosses the $\rho=0$ bisector in the negative angular direction ($p_\theta<0$). Due to the nature of the Hamiltonian phase space, the different surfaces of section corresponding to the different bisectors and directions contain the same information and no generality is lost in making the above choice.

Since we were unable to find a closed form solution to either the relativistic determining equation (12) or the equations of motion (16) and (17), it was necessary to employ numerical techniques to study the motion. Using a MATLAB integration routine (ode15s) we were able to solve the equations of motion in the N, pN, and R systems.

The ode15s routine uses a variable order method for solving stiff differential equations [23]. In order to control computational errors, we imposed absolute and relative error tolerances in the numerical routine of $\epsilon_{abs}=\epsilon_{rel}=10^{-8}$ so that the estimated error in each of the dynamical variables $\rho(i),\lambda(i),p_\rho(i)$, and $p_\lambda(i)$ at each step i in the numerical integration is

$$\epsilon(i) \leq \max[\epsilon_{rel}|y(i)|,\epsilon_{abs}], \qquad (37)$$

where $y(i)$ represents a generic, dimensionless dynamical variable at time step i. These dimensionless variables will be introduced shortly.

Furthermore, we periodically checked that the total energy of the system remained constant to ensure that the solution was stable and physically correct.

We found (both in this study and in Ref. [17]) that the numerical precision available to the computer did not allow the integration routine to solve the equations at energies approximately $H\gtrsim 2M_{tot}c^2$. We were unable to find a numerical integration routine that could integrate the equations of motion in this energy regime so the dynamics of the system at high energies still remains an open problem.

Furthermore, when we integrate the pN equations of motion, we find that the resulting energy of the numerical solution does not remain constant in time, despite the fact that the Hamiltonian (24) describes a conservative system. The variation in energy becomes greater as the differences between the masses increases. For the case when all masses are equal, this variation is on the order of the imposed numerical error tolerances and can be ignored. A description of the dynamics of the pN system in the equal mass case is given in Ref. [17]. The variation in energy increases drastically when we change the ratio of the masses even by a small amount. For example, when we integrate the equations of motion in the case where the mass of one particle is half that of the other two, we see a variation in the total energy on the order of $10^{-2}M_{tot}c^2$ over the duration of the trajectory. The cause of this energy variation is unclear but its magnitude is clearly too large to ignore. Due to this energy fluctuation, the numerical solutions to the post-Newtonian equations of motion

that we obtained in the unequal mass case are clearly unphysical and will not be presented in this paper.

We cast the expressions for the Hamiltonian and the equations of motion in the different systems in a dimensionless form using the coordinates $\hat{z}_i$ and $\hat{p}_i$, given by

$$z_i = \frac{4}{\kappa M_{tot}c^2}\hat{z}_i, \qquad (38)$$

$$p_i = M_{tot}c\hat{p}_i. \qquad (39)$$

We then express the dimensionless Hamiltonian as

$$\eta = \frac{H}{M_{tot}c^2} - 1, \qquad (40)$$

so that $\eta=0$ corresponds to H being equal to the total rest mass of the system. The total dimensionless energy for all systems is $\eta+1$ (recall that we are assuming the Newtonian Hamiltonian has been rescaled so that the zero point is the total rest energy of the system). In this way, a single value of η corresponds to the same energy in all three systems.

The equations of motion then become

$$\frac{\partial \eta}{\partial \hat{p}_i} = \frac{1}{c}\frac{\partial H}{\partial p_i} = \frac{4}{\kappa M_{tot}c^3}\frac{d\hat{z}_i}{dt} = \frac{d\hat{z}_i}{d\hat{t}}, \qquad (41)$$

$$\frac{\partial \eta}{\partial \hat{z}_i} = \frac{4}{\kappa M_{tot}^2 c^4}\frac{\partial H}{\partial z_i} = -\frac{4}{\kappa M_{tot}c^3}\frac{d\hat{p}_i}{dt} = -\frac{d\hat{p}_i}{d\hat{t}}, \qquad (42)$$

where we recognize $\hat{t}$ as the dimensionless time unit, given as

$$t = \frac{4}{\kappa M_{tot}c^3}\hat{t}. \qquad (43)$$

We refer to $\hat{t}=1$ as one time step. $\hat{\rho}$, $\hat{\lambda}$, $\hat{p}_\rho$, and $\hat{p}_\lambda$, the dimensionless counterparts of ρ, λ, p_ρ, and p_λ respectively, are defined as in Eqs. (25) and (26) using the hatted variables of Eqs. (38) and (39). In the subsequent analysis, dimensionless variables will be assumed unless otherwise stated.

V. SOLUTION TO THE EQUATIONS OF MOTION

In this section we present the results of our numerical analysis of the equations of motion. In Sec. V A we summarize the equal mass results of [17] then go on to present how the dynamics change in the unequal mass case in Secs. V B and V C.

A. Equal mass solution

The study of the N, pN, and R systems when all three particles share the same mass revealed a large variety of different types of trajectories. The different types of motion can be classified into three broad categories which we call annulus, pretzel, and chaotic. Note that our naming scheme is not standard in the literature of dynamical systems. Our nomenclature was chosen because of its direct physical interpretation in terms of the three particles (despite the fact

that the terms annulus and pretzel derive from the shape of the trajectories in the $\rho-\lambda$ plane).

Annulus trajectories correspond to the hex particle never crossing the same bisector twice in a row resulting in an orbit about the origin of the (ρ,λ) plane. The symbol sequence for all annulus orbits is $\bar{B}$. In terms of particles, these trajectories represent all motions in which no two particles cross successively. Most of the trajectories in this class never exactly repeat themselves after any number of orbits about the origin. The result is a densely filled region of the (ρ,λ) plane circling the origin. All of these trajectories form closed loops on a Poincaré map.

Pretzel trajectories are so named because of the complex patterns they make when plotted in (ρ,λ) coordinates. Symbolically, these trajectories fall into two distinct classes: (1) *regular* trajectories, which are denoted by some repeating pattern of A's and B's (e.g., $\overline{A^2B^{12}A^5B^3}$) and (2) *quasiregular* trajectories, represented by some repeating pattern of A's and B's with extra A motions occasionally occurring on each repetition of the pattern [e.g., $A^3(A^2B^6)^3A^2(A^2B^6)^{11}\ldots$]. As in the annulus case, most pretzel trajectories never exactly repeat themselves and densely fill a region of phase space. Pretzel trajectories appear either as a series of small enclosed loops or as a series of disconnected lines on a Poincaré map.

Chaotic trajectories are those that eventually cover all allowed regions of phase space and are denoted symbolically by an apparently random sequence of A's and B's. Since chaotic trajectories erratically cover a large region of phase space, they appear as densely filled regions on a Poincaré map. In all three systems there is a region of chaos separating the annulus and pretzel regions on the surface of section [17].

A comparison between the relativistic and Newtonian systems reveals differences in the trajectories as η increases. In general, the particles in the relativistic system cross each other at a higher frequency than in the Newtonian case for the same value of η. The structure of the relativistic Poincaré maps at all energies attainable were similar to the Newtonian ones except for a shifting of all trajectories to one side. Remarkably, this structure remained stable up to the values of η that were attainable despite the high degree of nonlinearity in the equations of motion.

Furthermore, for all trajectories studied in all three systems, B motion always occurred in multiples of 3 [17]. That is, all symbol sequences were of the form $\Pi_{i,j,k} (A^{m_i}B^{3n_j})^{l_k}$ so that any time a single particle, say particle 1, crossed the other two in succession, particles 2 and 3 always crossed next before meeting particle 1 again.

B. Unequal mass trajectories

In order to study the effects of changing the relative masses of the particles, we adopt the parameter α whenever two masses are equal so that $m_1=m_2=\alpha m_3$. When all three masses are unequal, we will describe the relative masses as a ratio (i.e., $m_1:m_2:m_3=1:2:3$).

In the case when two masses are equal ($\alpha \neq 1$), we find the same diversity of trajectories in the (ρ,λ) plane as in the $\alpha=1$ case [17]. Figure 6 shows this diversity for different
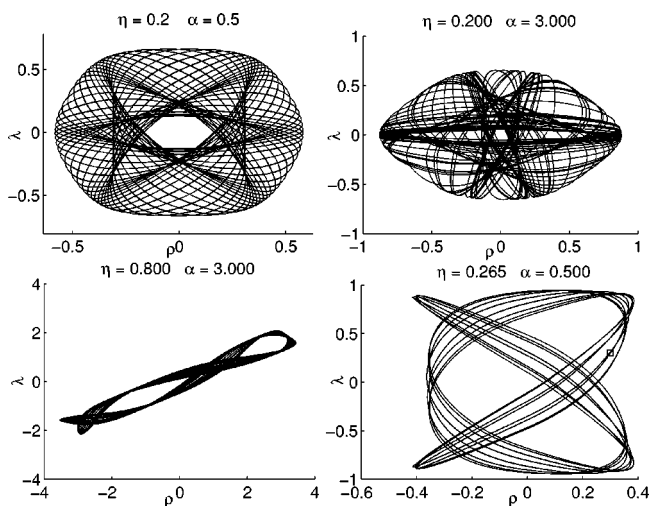

FIG. 6. Examples of trajectories in the N system for different values of η and α. Each trajectory was run for 150 time steps. The small box indicates the starting position of the trajectory. Proceeding clockwise from the top left plot the symbol sequences are $\bar{B}$, $\bar{B}$, $\overline{AB^3A^2B^3}$, and $\overline{B^6AB^9A}$.

values of α in the N system while Fig. 7 and 8 show examples of annulus and pretzel trajectories, respectively, for the R system. Similar trajectories are obtained when all three masses are unequal.

In terms of the hex particle moving in the ρ-λ plane, we did not find a significant difference between the equal and unequal mass trajectories besides a general distortion of the annulus orbits as the difference in masses increases. For instance, in the equal mass case [17], all of the annulus orbits were generally hexagonal about the origin. When the mass of one particle is larger than the rest, these annuli take on a more boxlike shape, as can be seen in Fig. 7. Besides a general distortion, we did not find any novel types of motion that were not seen in the equal mass case. Since the qualita-
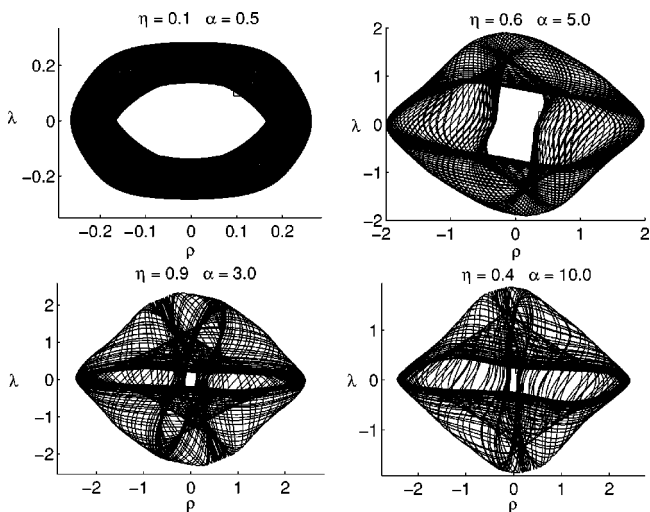

FIG. 7. Examples of relativistic annulus trajectories for different values of η and α. Note the characteristic boxy shape at higher values of α. Each trajectory was run for 200 time steps. All trajectories have the symbol sequence $\bar{B}$.
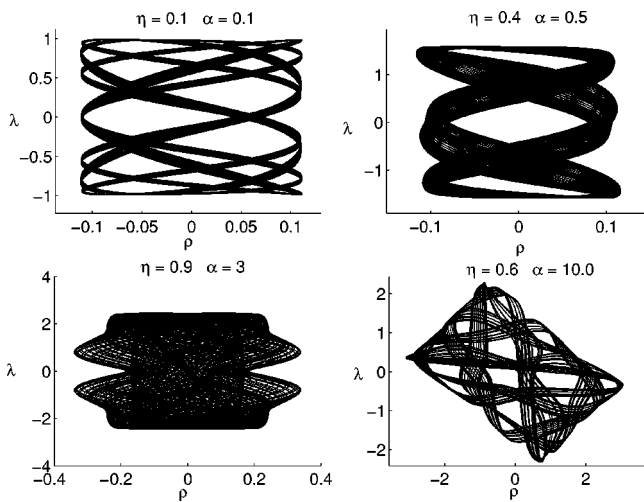
FIG. 8. Examples of relativistic pretzel trajectories for different values of η and α. Each trajectory was run for 200 time steps. The top right plot has symbol sequence $\overline{A^2B^3}$.

tive aspects of the motion in the ρ-λ plane do not reveal much about the underlying physics, we will forgo any further discussion on this matter.

Another effect of changing the difference between the particle masses is that the ratio between the number of annulus trajectories compared to the number of pretzel orbits at a given energy decreases. That is, as α decreases, we find fewer and fewer initial conditions that give annuli compared to initial conditions that produce pretzels. The reason for this is best demonstrated by looking at the motion of the particles as a function of time.

Figure 9 plots the relative motion of the particles for decreasing values of α in the R system for a specific set of initial conditions. We see that, at equal mass ($\alpha=1$), a single particle alternately crosses the other two without ever crossing the same particle twice, indicative of annulus motion. However, as α decreases, the mass of particle 3 decreases and so its frequency of oscillation decreases while its amplitude increases with respect to the other two.

In effect, we see that the two massive particles gravitationally bind together more tightly as the difference between their mass and the mass of the third particle increases. Eventually, this binding becomes so tight that the two massive particles are forced to execute an additional A motion before crossing the third particle and, hence, there is a transition from annulus type motion to pretzel type motion. This behavior, while expected for the Newtonian system (Fig. 10), is also present in the relativistic case.

As the mass difference increases, it is much more difficult to set up initial conditions at a given energy such that particle 1 and 2 do not cross more than once during one of particle 3's long period oscillations. This effect is also seen in the Newtonian system, as shown in Fig. 10. This difference in the ratio of the number of annulus trajectories compared to pretzel trajectories will be made more clear in the following section when we look at the Poincaré maps.

Using these position-time plots, it is interesting to explore the limit where one mass is much greater and much smaller than the other two ($\alpha \gg 1$ and $\alpha \ll 1$, respectively). The
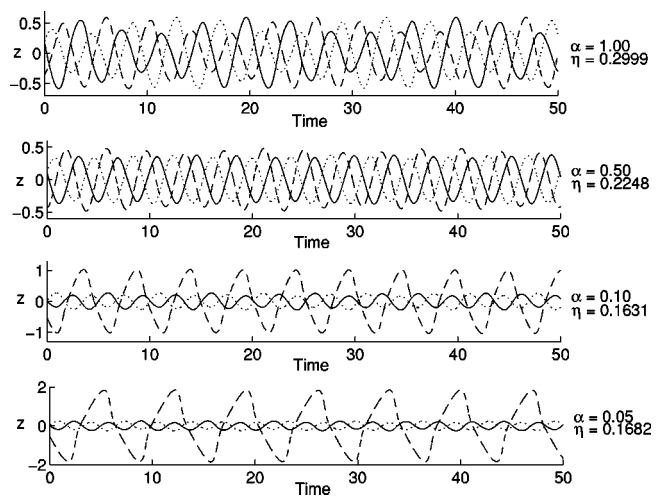

FIG. 9. The relative position of each particle with respect to the center of mass is plotted as a function of time for various values of α in the R system. The particles 1, 2, and 3 have relative masses in the ratio $1:1:\alpha$. Solid line—particle 1, dotted line—particle 2, and dashed line—particle 3. Each plot uses the same initial values of $(\rho,\lambda,p\rho,p\lambda)$ but the total energy $\eta+1$ is fixed by the energy constraint (12). The top two plots display annulus motion ($\overline{B}$) while the bottom two are classified as pretzel trajectories [$\overline{(B^6A)^7B^3}$ and $\overline{A^2B^3(AB^3)^5}$, respectively].

former case is shown in Fig. 11 for the N and R systems where $\alpha=100$. In both cases, as one would expect, we see the large mass barely moves while the other two particles oscillate about it. The inset shows the small perturbations to the motion of the larger mass caused by the passing of the two particles. In the Newtonian case, the perturbation is very smooth and regular while the perturbation in the relativistic case is more jerky and erratic. That is, the velocity of the
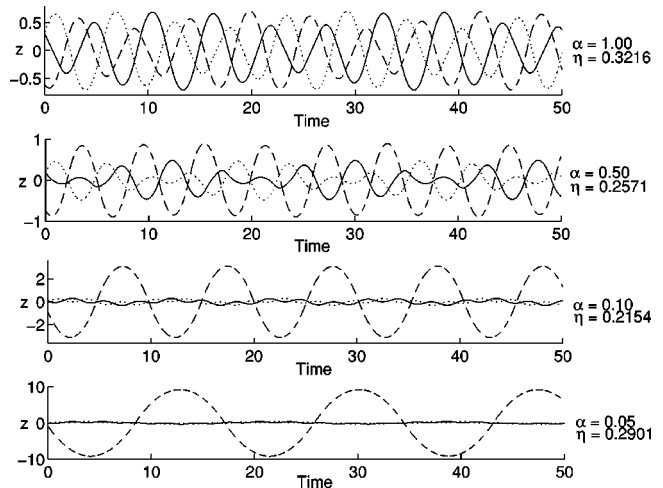

FIG. 10. The relative positions of each particle with respect to the center of mass as a function of time in the N system. These plots were created using the same procedure as in Fig. 9 and follow the same conventions except that Eq. (20) is used to fix the value of the total energy η. The first is an annulus trajectory ($\overline{B}$) while the remaining are pretzels [$\overline{B^9A}$, $\overline{(B^3A^2)^4B^3A^3}$, and $\overline{(B^3A^5)^2B^3A^4}$ from top to bottom].
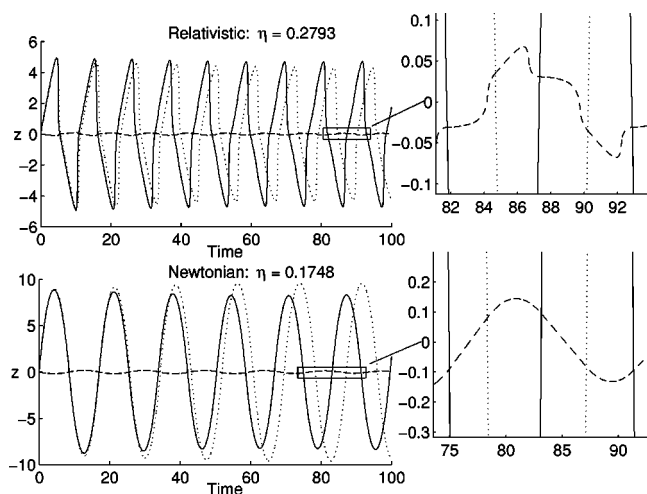
FIG. 11. Relative motion of the particles with respect to the center of mass plotted as a function of time for the R system (top) and the N system (bottom). Both plots have mass ratios $1:1:100$ or $\alpha = 100$. The lines are as defined in Fig. 9. The insets show the small perturbation in the motion of the large mass due to the crossing of the smaller masses.

large mass in the R system increases much more suddenly than in the N system when it encounters another smaller mass.

Figure 12 shows the corresponding plots when $\alpha = 0.01$. We see that, in both cases, the two heavy particles form a stable, two-body subsystem while the third particle oscillates about their center of mass. As seen in the upper most insets in both the R and N case, the presence of the light particle has a weak gravitational effect, causing the oscillatory motion of the center of mass of the two more massive particles. Unlike the effect seen in Fig. 11, the perturbation of the motion of the heavy particles due to the crossing of the light particle is very small in the R system and almost impercep-
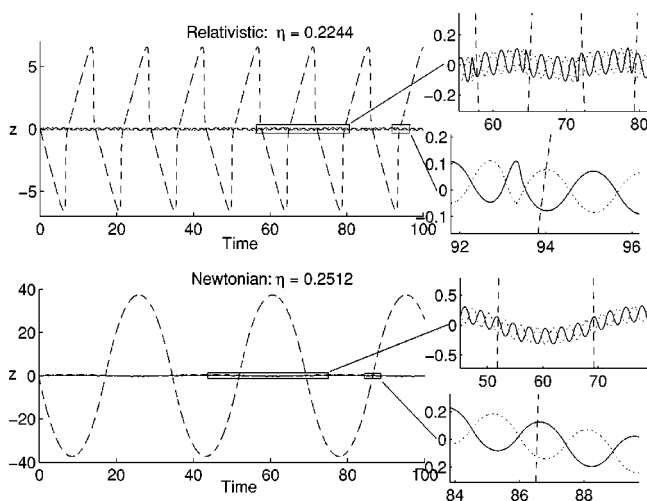

FIG. 12. Relative motion of the particles for the case where the mass ratio is $1:1:0.01$ or $\alpha = 0.01$ for both the R (top) and N (bottom) systems. The insets show the motion of the stable, two body subsystem made up of the two heavy particles, as well as the effect of encounters with the light particle.
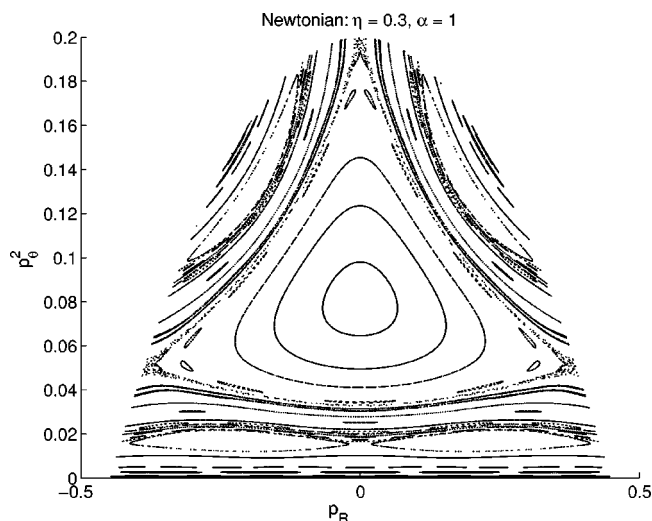

FIG. 13. A Poincaré map of the Newtonian system when all of the particle masses are equal.

tible in the N system. The reason for this is that the two heavy particles in the $\alpha = 0.01$ case are twice as massive as the single particle in the $\alpha = 100$ and so the motion of the two-body subsystem is much more stable and less susceptible to harassment from the weaker mass. However, the qualitative nature of the perturbation remains the same as in the $\alpha = 100$ case.

We also find that the amplitude of oscillations in the Newtonian system is generally larger than in the relativistic system at corresponding values of the total energy and that the frequency of oscillations is greater in the relativistic case. These observations agree with the results found in the equal mass case [17].

Finally, we note that, as in the equal mass case, we find that B motion always comes in multiples of three. That is, the symbol sequence always takes the form

$$\prod_{i,j,k} (A^{m_i}, B^{3n_j})^{l_k}, \tag{44}$$

for all values of α and η that were studied. This extends our hypothesis proposed in Ref. [17] that all trajectories in the R and N systems, when translated into a symbol sequence, have the form (44), to also hold for all mass ratios of the three particles.

C. Global structure of phase space

By studying the two-dimensional representations of phase space represented in the Poincaré maps we were able to discover some interesting global properties of both the N and R systems. We begin this section by describing some of the basic features of the Poincaré plots and then go on to discuss how the structure of phase space changes when the mass ratio of the particles is changed. Our results will then be compared with similar studies conducted previously.

An example of a Poincaré map for the N system when all masses are equal is shown in Fig. 13. All points on this surface of section fall within a parabolic region which is
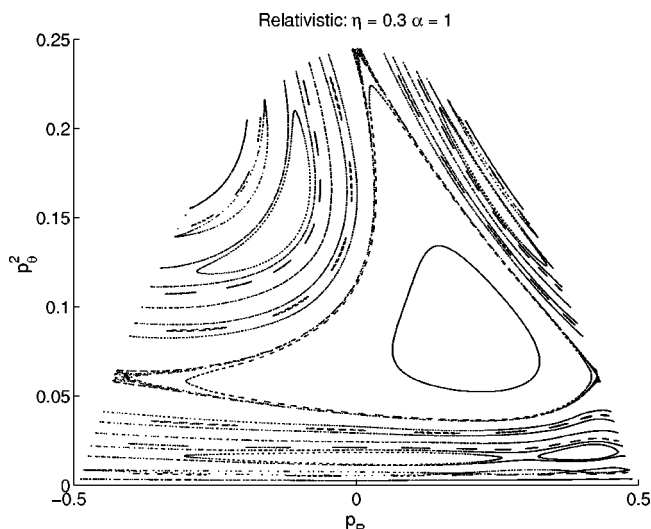
FIG. 14. A Poincaré map of the relativistic system when the masses of all of the particles are equal.

defined by the system's energy constraint. It was found in Ref. [17], as mentioned previously, that the three types of motion, annulus, pretzel, and chaotic, fall into three regions on the surface of section. Quasiperiodic annulus orbits form single closed loops about a stable fixed point at which the motion is completely periodic. In Fig. 13 this region of quasiperiodic annuli is located at the center of the plot enclosed within the densely filled triangular shaped region. This densely filled region is created by chaotic trajectories and separates the annulus region from the pretzel region. All pretzel trajectories fall outside of this chaotic region and form either a series of disconnected loops or a series of disconnected lines.

A similar segregation of the surface of section is also seen in the R system, an example of which is shown in Fig. 14. The relativistic Poincaré map is strikingly similar to the Newtonian one in Fig. 13. The annulus region is shown as

the series of closed loops in the lower right portion, surrounded by the warped chaotic region, which is further surrounded by the region of pretzel trajectories.

In general, the relativistic phase space is a warping of the corresponding Newtonian space. As described in Ref. [17], this is due to the weaker symmetry of the relativistic Hamiltonian compared to the Newtonian. As seen in Eq. (20), the N system is invariant under the symmetry $p_i \to -p_i$ and this is manifest in the symmetry about the $p_R=0$ axis in Fig. 13. The relativistic Hamiltonian, determined by Eq. (12), is invariant under the symmetry $(p_i, \epsilon) \to (-p_i, -\epsilon)$. Contrary to the Newtonian case, this relativistic symmetry is not manifest in our surface of section.

We find that the annulus and pretzel trajectories continue to fall into similar regions, as described above, for all different mass ratios studied, and that these two regions are always separated by a region of chaos. By changing the mass ratio at a given value of the total energy, the size and shape of the different regions change.

More specifically, by looking at the case where particles 1 and 2 share the same mass, the annulus region becomes smaller and moves towards the top of the allowed region of the surface of section with decreasing $\alpha < 1$ as can be seen in Fig. 15 for $\alpha=0.1$ in both the N and R systems. This shrinking of the annulus region is a manifestation of the effect discussed in Sec. V B where annulus motion becomes more difficult to attain when one particle is significantly less massive than the other two.

As α increases, the annulus region extends towards the lower region of the plot, as shown in Fig. 16 for $\alpha=10$ in both the R and N systems. Essentially, this means that one requires a lower magnitude of angular momentum of the hex particle to attain an annulus orbit in the ρ-λ plane. Since the gravitational attraction between the two light particles is not very strong compared to their interaction with the heavy particle, the light particles do not tend to oscillate about each other very much but instead act like two separate two body systems with the heavy particle taking the role of the second body, like a two-planet, one-dimensional solar system. This situation is shown in Fig. 11 for $\alpha=100$ and explains why
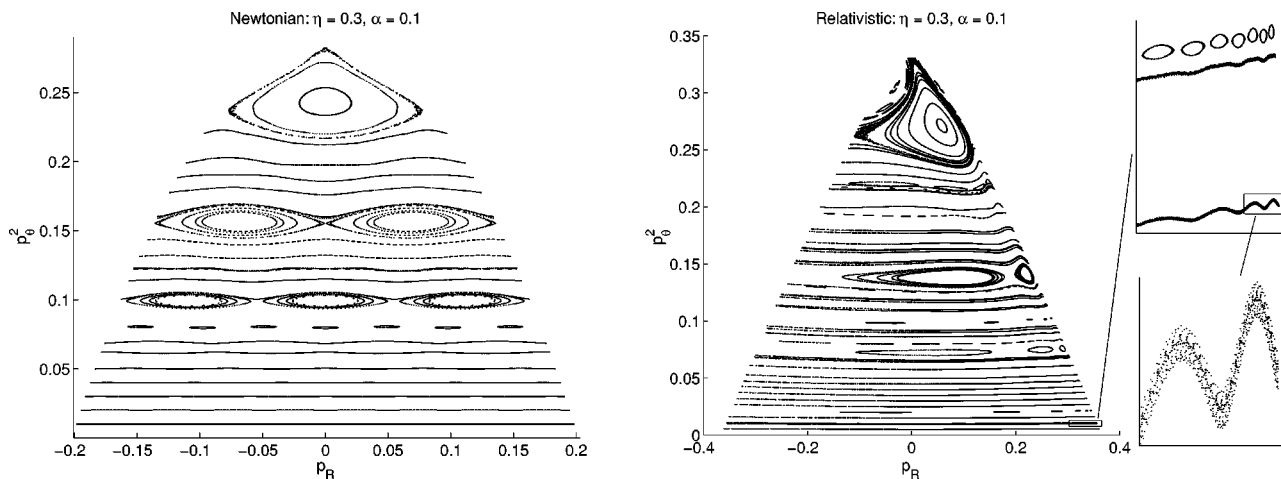

FIG. 15. Poincaré plots with $\alpha=0.1$ for the Newtonian (left) and relativistic (right) systems. The insets on the right show the onset of chaos in the pretzel region.
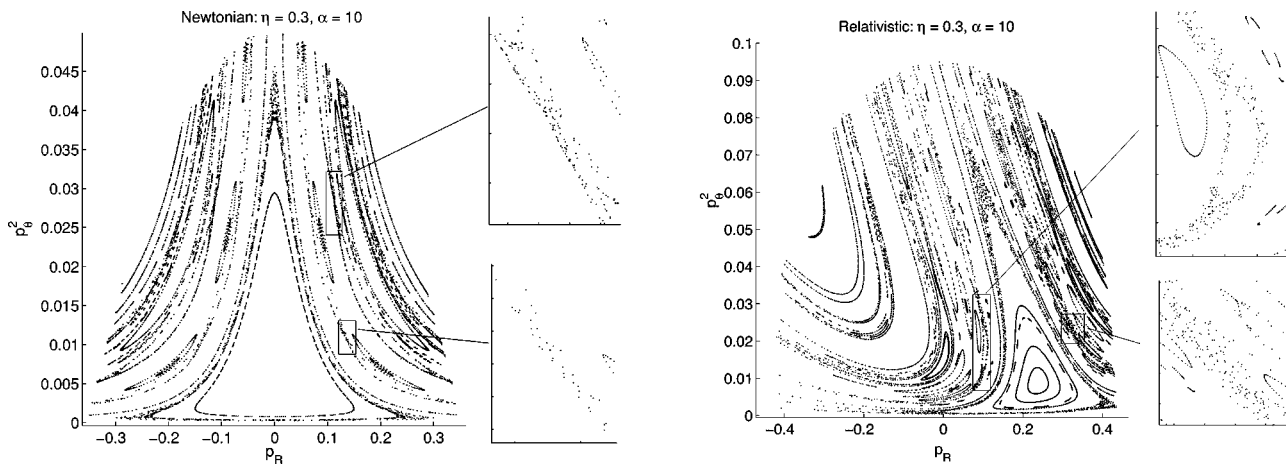
FIG. 16. Poincaré plots with $\alpha=10$ for the Newtonian (left) and relativistic (right) systems. The insets show additional regions of chaos in the pretzel region that are not present in the corresponding region on the equal mass Poincare section.

there is no decrease in size of the annulus region with increasing α.

The symmetry about $p_R=0$ present in Figs. 15 and 16 is really just an artifact of our choice of surface of section. Recall that we chose to construct our Poincaré maps by plotting a point each time the hex particle crossed the $\rho=0$ bisector, or, equivalently, each time particles 1 and 2 crossed. The above figures were constructed with $m_1=m_2$ and so the symmetries of the equal mass system persist. If we were to have chosen a different bisector, all of the features discussed above would remain (e.g., shrinking, expanding of annulus region) but these would not occur in the same sense and the plots would not be as symmetrical.

This can be shown by creating Poincaré maps for the case when all three masses are unequal. An example for both the R and N system is shown in Fig. 17 where the mass ratio is $m_1:m_2:m_3=1:5:10$. Here we see that the symmetry about

the $p_R=0$ axis no longer exists in the Newtonian system due to the fact that none of the particles have equal mass. We also see a further warping of the relativistic plots due to this added asymmetry. Furthermore, we find that the different regions are not as clearly segregated as in the $m_1=m_2$ phase space but extend over more of the Poincaré map. For instance, in the relativistic map of Fig. 17 we see that the chaotic region separating the annulus and pretzel trajectories [marked by (1)] is no longer a single, densely filled loop but actually two loops which were created by a single trajectory. The annulus region is confined to the area inside both of these loops, where a single annulus trajectory will visit both regions.

Besides this novel partitioning of the different regions, the changes to the structure of the phase space for different ratios of the mass when all three masses are unequal are analogous to the results described above for the case where $m_1=m_2$. For
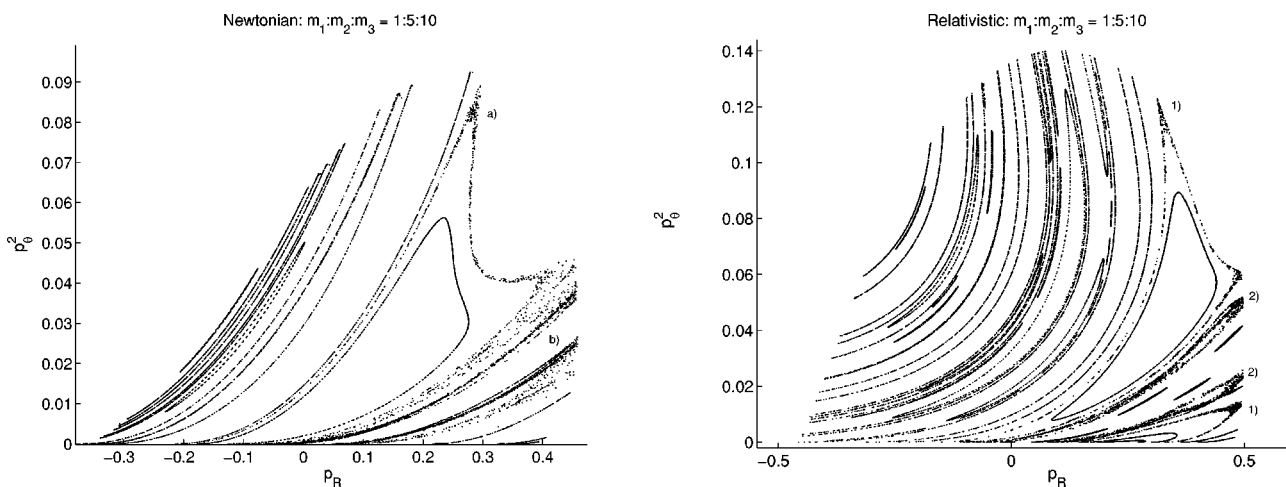

FIG. 17. Poincaré plots with a mass ratio of $1:5:10$ for the Newtonian (left) and relativistic (right) systems. On the left, (a) marks the region of chaos separating annulus trajectories (inside) and predominantly pretzel trajectories (outside) while the densely filled area directly above and below (b) marks a new region of chaos amongst the pretzel trajectories. On the right, the densely filled regions marked by a (1) were created by a single trajectory separating the annulus and pretzel orbits while the chaotic regions marked by (2) were created by a trajectory within the pretzel region.

example, the ratio 1:5:10 exhibits similar behavior as the case when there is one light particle and two heavy ones, only the effects are not as prevalent because of the intermediate mass particle. The results can be seen as an interpolation between the 1:1:1 case and the 1:10:10 case.

One major difference that we find between the equal and unequal mass cases is the presence of additional chaotic regions in the unequal mass space that are not present in the corresponding constant energy hypersurface of the equal mass space. This is true for both the Newtonian and relativistic systems. For the mass ratios and energy levels that we have studied, these additional chaotic regions appear within the pretzel regions of the corresponding equal mass surface of section. The novel chaotic trajectories are characterized by broadened lines in the pretzel region as can be seen in Figs. 15–17. The exact physical mechanism that gives rise to this increase in chaos is not presently known.

Note that, although there are no apparent regions of chaos in the Newtonian, $\alpha=0.1$ Poincaré map of Fig. 15 (besides the one separating the annuli from the pretzels), we do find a slight broadening of lines in the other two Poincaré maps constructed by plotting points each time the hex particle crosses the other two bisectors, respectively.

That is, additional regions of chaos do form in the unequal mass phase space but these new regions cannot be seen on the particular choice of Poincaré section shown in Fig. 15. We suspect that these new regions of chaos would become more prevalent as the difference in particle masses increases.

It is instructive to compare our results with a similar study of a billiard in R^2 colliding with a wedge in a uniform (Newtonian) gravitational field performed by Lehtihet and Miller (referred to as LM herein) [2]. LM showed that the two-dimensional wedge billiard system is isomorphic to a system of three elastically colliding, self-gravitating particles (under Newtonian gravity) in one-dimension, with the relative masses of the particles directly related to the wedge angle by

$$\tan \theta = \frac{\sqrt{1 + 2\alpha^{-2}}}{1 + 2\alpha^{-1}}, \tag{45}$$

where α is as defined in our study. LM only considered the situations where the wedge is symmetric, which corresponds to the case when two of the three masses are the same. The value of $\theta=\pi/6$ corresponds to $\alpha=1$, the equal mass case. This connection between particle masses and the wedge angle agrees with the distortion of the potential energy described in Sec. III where the angle of the wedge is related to the angle between the bisectors of the hexagonal well.

The only difference between the LM system and our N system is the existence of collisions in the former while the particles pass through each other in the latter. For the case where all three particles are identical, it is irrelevant whether one considers that the particles are colliding or passing through each other (besides the question of labeling the particles). For this reason, the phase space structure of the Newtonian equal mass configuration, as presented in the Poincaré

maps, is identical between our system and the wedge-billiard system.

LM found that this wedge-billiard system exhibits the characteristics of a conservative Hamiltonian system with two degrees of freedom and a discontinuity. By changing the value of a single continuous parameter θ they found a variety of dynamics similar to our study. More specifically, for $\theta<\pi/4$ (which corresponds to the entire range of physical values of α) they found that integrable, near integrable, and chaotic regions coexisted in phase space. Furthermore, as the wedge angle was increased from $\pi/6$ [corresponding to both an increase *or* a decrease of α due to the nature of the connection between mass ratio and wedge angle (45)], they found that the region surrounding periodic fixed points was consumed by regions of simply connected chaos which increased in size with increasing wedge angle.

As noted above, we find a similar behavior in both our Newtonian and relativistic systems in that we see an increase in the amount of chaos as the difference in the masses increases. However, we have only studied moderate particle mass differences in order to characterize the general nature of the unequal mass system and it is not clear how the global structure of our system will behave for very large differences in the particle masses. In particular, we do not know if our systems will experience a global transition to chaos or if there exists integrable and near integrable regions for all mass ratios. This remains an area for further study.

VI. DISCUSSION

We have presented the results of a continued study of the three-body problem in lineal gravity begun in Refs. [16,17]. The focus of the present investigation was to see what happens to the motion of the particles when the relative masses of each are not equal. Here we summarize our results.

The derivation of the three-body Hamiltonian by canonical reduction of the action (1) was summarized and the associated post-Newtonian and Newtonian Hamiltonians presented. Each Hamiltonian possesses two spatial degrees of freedom with two conjugate momentum degrees of freedom and these were made manifest by changing to (ρ,λ) coordinates. Expressions for the potential energy of each system were derived and the distortion of the potential energy due to varying the mass ratio was described.

The results of the study of the equal mass case were summarized and the different types of motion were classified into three categories: annulus, where each particle always crosses the other two in succession; pretzel, in which two particles can cross each other twice in a row; and chaotic, where the sequence of particles crossings does not progress in a discernible pattern. By studying the motion of the three particles and their corresponding hex-particle representation in the ρ-λ plane, we characterized how changing the mass ratio of the particles effects the dynamics of the system. More specifically, we described in physical terms how the type of motion (annulus, pretzel, and chaotic) and their relative abundance in phase space changes with respect to the mass ratio.

As the relative difference between the masses of the particles increases, we find the onset of additional regions in phase space of chaos that are not present in the equal mass system—in other words, we find that motion that was once quasiperiodic is now chaotic. This shows that the unequal mass phase space is not simply a deformation of the corresponding equal mass space but, indeed, contains novel dynamics. The physical mechanism behind this phenomenon is currently unknown.

This is similar to the behavior of a billiard colliding with a wedge (which is isomorphic to three particles elastically colliding on a line under their mutual, Newtonian attraction) studied by Lehtihet and Miller [2]. It is still not known what happens to these novel regions of chaos as the difference in mass gets exceedingly large.

There are still many open areas of study in the lineal, three-body problem. As was done in the two-body problem [8–11] it will be interesting to see the effect of adding charge to the particles and a cosmological constant to the system. Furthermore, more sophisticated numerical techniques need to be introduced in order to probe the dynamics of the system at high energies and in order to study the motion in the post-Newtonian system for unequal mass particles. A description of the global structure of phase space for extreme differences in the particle masses is still needed in order to determine the stability of the system in these limiting cases. As mentioned above, a discrete map between particle crossings in the N and R systems (although it is doubtful whether this can be obtained for the latter) may illuminate some of the more general features of the three-body system. The development of a relativistic three-body system where the particles elastically collide instead of passing through each other would also be an interesting subject to study to see if the increased chaos reported in Ref. [2] has an analog in the relativistic system.

[1] See B. N. Miller and P. Youngkins, Phys. Rev. Lett. **81**, 4794 (1998); K. R. Yawn and B. N. Miller, *ibid.* **79**, 3561 (1997), and references therein.

[2] H. E. Lehtihet and B. N. Miller, Physica D **21**, 93 (1986).

[3] G. Rybicki, Astrophys. Space Sci. **14**, 56 (1971); H. L. Wright, B. N. Miller, and W. E. Stein, *ibid.* **84**, 421 (1982), and references therein.

[4] N. D. Whelan, D. Goodings, and J. K. Cannnizzo, Phys. Rev. A **42**, 742 (1990).

[5] D. Bukta, G. Karl, and B. Nickel, Can. J. Phys. **78**, 449 (2000).

[6] H. Koyama and T. Kinoshi, Phys. Lett. A **279**, 226 (2001).

[7] T. Ohta and R. B. Mann, Class. Quantum Grav. **13**, 2585 (1996).

[8] R. B. Mann and T. Ohta, Phys. Rev. D **57**, 4723 (1997); Class. Quantum Grav. **14**, 1259 (1997).

[9] R. B. Mann, D. Robbins, and T. Ohta, Phys. Rev. Lett. **82**, 3738 (1999).

[10] R. B. Mann, D. Robbins, and T. Ohta, Phys. Rev. D **60**, 104048 (1999).

[11] R. B. Mann, D. Robbins, T. Ohta, and M. Trott, Nucl. Phys. B **590**, 367 (2000).

[12] R. B. Mann and T. Ohta, Class. Quantum Grav. **17**, 4059 (2000).

[13] R. B. Mann and P. Chak, Phys. Rev. E **65**, 026128 (2002).

[14] R. B. Mann, Class. Quantum Grav. **18**, 3427 (2001).

[15] R. Kerner and R. B. Mann, Class. Quantum Grav. **20**, L135 (2003).

[16] F. J. Burnell, R. B. Mann, and T. Ohta, Phys. Rev. Lett. **90**, 134101 (2003).

[17] F. Burnell, J. J. Malecki, R. B. Mann, and T. Ohta, Phys. Rev. E **69**, 016214 (2004).

[18] R. B. Mann, Phys. Lett. A **4**, 425 (1991); R. B. Mann, Gen. Relativ. Gravit. **24**, 433 (1992).

[19] S. F. J. Chan and R. B. Mann, Class. Quantum Grav. **12**, 351 (1995).

[20] R. Jackiw, Nucl. Phys. B **252**, 343 (1985); C. Teitelboim, Phys. Lett. **126**, 41 (1983).

[21] B. N. Miller and K. Ravishankar, J. Stat. Phys. **53**, 1299 (1988).

[22] J. Hietarinta and S. Mikkola, Chaos **3**, 183 (1993).

[23] L. F. Shampine and M. W. Reichelt, SIAM J. Sci. Comput. (USA) **18**, 1 (1997).